Simulation of Plasma–Water Interaction with Discharge in the Existing Bubble in Water

N. Mohammadi Nahrani[a], M. Bahreini[a,*] and S. Hasanpour Tadi[b]

[a] *School of Physics, Iran University of science and technology, Resalat Square, Hengam Street, 13114-16846, Tehran, Iran*
[b] *Laser and plasma research institute, Shahid Beheshti university, Evin, Shahid Shahriari Square, 1983969411, Tehran, Iran*

Received: 06.11.2022 & Accepted: 01.12.2022

Doi: 10.12693/APhysPolA.143.100 *e-mail: m_bahreini@iust.ac.ir

In plasma technology, the plasma–liquid interaction is a significant issue. In this work, finite element methods are used to simulate a 2D dielectric barrier discharge and an arc discharge to investigate the simulation of discharge in spherical bubbles in the water that formed plasma-activated water. Different periods are examined to determine how the electron density changes with voltage, frequency, dielectric thickness, and bubble radius. The results demonstrated that increasing voltage, frequency, bubble radius, and decreasing dielectric thickness increase electron density linearly. The increasing rate of electron density by time evolution is investigated while voltage is constant in the generation of arc discharge. High plasma density indicates sufficient plasma–water interaction.

topics: plasma–liquid interaction, plasma bubble discharge, arc discharge simulation

1. Introduction

The term "plasma" refers to a quasi-neutral ionized gas made up of excited and neutral atoms, as well as photons, ions, and free electrons [1]. There are two types of plasma: thermal and non-thermal (cold plasma). Thermal plasma belongs to thermal equilibrium conditions, which means that both electrons and ions are at the same temperature obtained by high energy consumption. The plasma is non-thermal (cold) when the temperature of the electrons is significantly higher than that of the ions, and it does not require as much energy to produce as the thermal plasma does [2].

Plasma has a wide range of applications, for example, in medical fields [3] and medical diagnosis [4, 5], in disinfection and sterilization [6–8], cancer treatment [9], wound healing [10], and skin rejuvenation [11]. In the fabric industry, plasma is used to increase strength, water repellency, and fabric dyeability [12]. In agriculture [13] and the food industry [14], plasma is involved in sterilization, pesticide, seed germination, and plant growth [15]. It is also tested for controlling emissions of industrial pollution [16, 17]. For nanoparticle synthesis, the plasma-generated AgNPs are well-dispersed in the presence of the geminin cationic surfactant, and the nano-surfactant compounding system has been improved for antibacterial activity as well as good stability [18]. Another application is the material analysis by a plasma discharge, called spark [19].

Furthermore, one of the most important plasma applications is water treatment, which is used in various fields, including bio-sterilization, decontamination, industrial waste [20], agriculture, and water purification [21].

Despite its challenges, the interaction of plasma and liquid is becoming an important topic in the field of plasma technology [22]. There are various types of plasma–liquid interactions depending on the discharge mechanism:

1. direct discharges in liquids classified as strong field discharges, such as laser pulses (Fig. 1) [22];
2. discharges over a liquid in the gaseous phase, including both indirect and direct contact with the liquid (Fig. 2) [22];
3. discharges in multi-phase environments, such as discharges inside liquid bubbles or discharges coming into touch with liquid sprays or foams. This interaction causes some instabilities that result in bubble production and imprint the initial micron-sized bubbles (Fig. 3).

One of the aforementioned electrical discharge methods is capable of producing the useful byproduct of this interaction, i.e., plasma-activated water (PAW) [23]. In plasma-activated water, reactive oxygen species (ROS) and reactive nitrogen species (RNS) are produced [24, 25]. The reactive oxygen

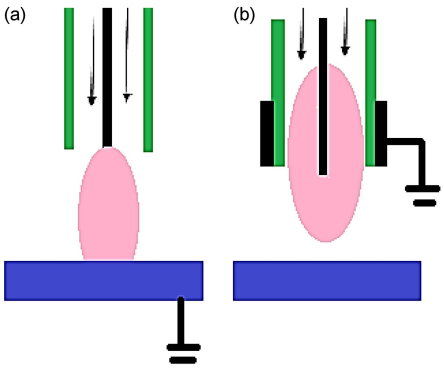

Fig. 1. Indirect liquid discharges; (a) pin-to-water, (b) atmospheric pressure plasma jet (APPJ) geometries.

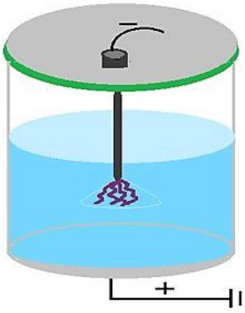

Fig. 2. Direct liquid discharge; an example of the pin-to-plate geometry.

and nitrogen species (RONS) in PAW include long-lived species such as nitrate (NO_3^-), nitrites (NO_2^-), hydrogen peroxide (H_2O_2), and ozone (O_3) besides short-lived species such as hydroxyl radicals (OH), nitric oxide (NO), superoxide (O_2^-), peroxynitrite ($OONO_2^-$), and peroxynitrite ($ONOO^-$) [26]. The synthesis of RONS active species allows PAW to be used in a variety of applications [26]. RONS are used for cancer cell treatment [27] and as facilitation in agricultural applications of PAW [28], such as increased seed germination and plant growth [29], due to the role played by reactive species like NO_2^-, NO_3^-, H_2O_2, and NH_3 [30]. It is also used in food industries [22] for the disinfection of fruits and vegetables, regulation of enzymes and pesticides in the presence of RNS species, as well as dental treatment, wound healing, and cancer treatment [31].

Additionally, it takes specialized and expensive research to examine and analyze chemical reactions in electrical discharge via water. There are some studies in plasma–liquid interaction simulation. N. Vichiansan et al. [32] simulated a plasma jet for NO, OH, and H_2O_2 production in a simple 2D model and they measured the densities of H_2O_2 and OH at a distance of 5 mm and 10 mm, respectively. A. Wright et al. [33] simulated a dielectric barrier discharge (DBD) plasma reactor at the gas-liquid interface in 2D asymmetric geometry and in-

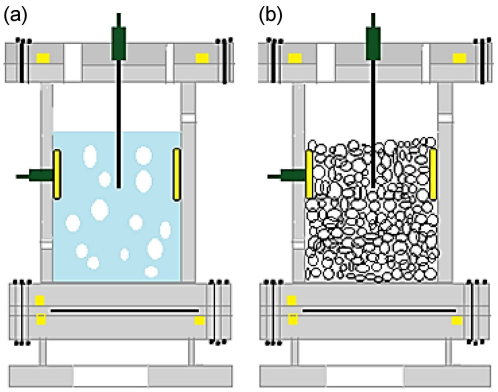

Fig. 3. Multiphase plasma–liquid discharge; discharges contacting liquid sprays or foams.

vestigated the effect of the membrane type on the plasma characteristics and the effect of electrode type on size of the bubble. In this investigation, two types of steel and nickel layers were considered, with the steel layer 1.75 times larger than the nickel layer. The measurement of long-lived species concentrations was performed by Fourier-transform infrared spectroscopy (FTIR) and UV absorption spectroscopy methods [33]. Y. Wang et al. [34] used the COMSOL software to model a gas phase surface discharge plasma reactor simulation for yeast inactivation in water and determine the effect of reaction rate coefficient (kreac) on the initial concentration of yeast cells. They have shown that the amount of kreac decreases with increasing the initial concentration [34]. Zhihang Zhao et al. [35] simulated the surface dielectric barrier discharge (SDBD) at low temperatures and sub-atmospheric pressure. Under a DC voltage of 12 kV, with the propagation of the streamer, the parameters such as electron density, N^{+2} density, N_2 density, O^{-2} density, electron temperature, space charge density, electric field, and photoionization rate were studied [35].

Since PAW has a variety of applications, simulation of the plasma-water interaction is an important topic that has been addressed in this work. Direct discharge inside of liquids appears to be impractical since it requires a lot of power to produce the desired effects at high voltages and high-power levels. As a result, employing water bubbles allowed us to achieve more realistic results using standard discharge devices. In this study, electrical discharge within bubbles has been investigated as a noble model. Two structures of the pin-to-pin arc discharge and the dielectric barrier discharge (DBD) are used to simulate electrical discharge in water using the finite element method by COMSOL software (version 6.0). The multiphase discharge used argon as the inlet gas, and the formation of bubbles from plasma was assessed. The simulation considers 2D numerical models with these structures and uses quartz as a dielectric, while the inside of the bubbles is filled with argon gas immersed in water.

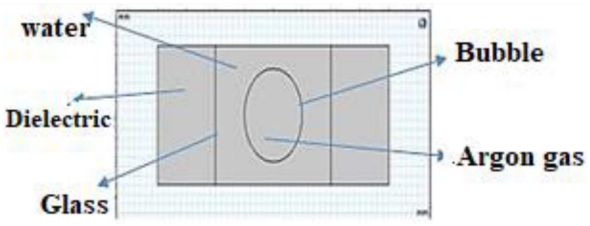

Fig. 4. The schematic diagram of the 2D simulation model with a single bubble.

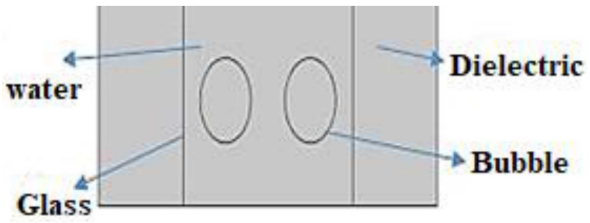

Fig. 5. Simulated model of two consecutive bubbles with a radius of 0.06 mm.

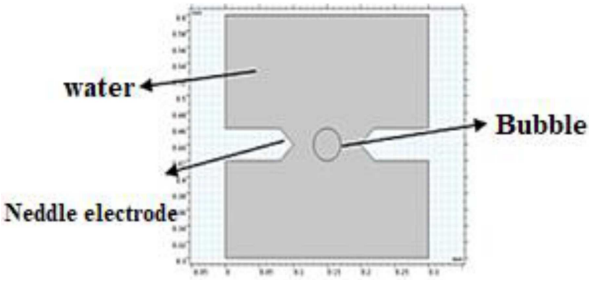

Fig. 6. Schematic of the 2D simulation of arc discharge structure.

The results include the distribution of electron densities, discharge voltage, operating frequency, bubble radius, dielectric thickness, and argon ions at a pressure of 1 atm and temperature of 293 K.

2. Material and method

2.1. Description of modeling geometry

This simulation considers 2D numerical models with a DBD structure, uses quartz as a dielectric with a permittivity of 4.5, and the inside of the bubbles is filled with argon gas immersed in water. Due to charge conservation, the boundary between the electrode and the water is regarded as a glass dielectric in geometry, and plasma only forms inside the bubble. Two different geometries are shown in Figs. 4 and 5.

In addition to dielectric barrier discharge, arc discharge has also been simulated using the same boundary conditions. The geometry is shown in Fig. 6, which presents a single bubble with a radius of 0.01 mm.

TABLE I

Table of collisions and chemical reactions in the simulated model.

Formula	Type	$\Delta\varepsilon$[eV]
$e + \mathrm{Ar} \Longrightarrow e + \mathrm{Ar}$	elastic	0
$e + \mathrm{Ar} \Longrightarrow e + \mathrm{Ars}$	excitation	11.5
$e + \mathrm{Ar} \Longrightarrow e + \mathrm{Ar}$	superplastic	−11.5
$e + \mathrm{Ar} \Longrightarrow 2e + \mathrm{Ar}^+$	ionization	15.8
$e + \mathrm{Ars} \Longrightarrow 2e + \mathrm{Ar}^+$	ionization	4.28
$\mathrm{Ars} + \mathrm{Ars} \Longrightarrow e + \mathrm{Ar} + \mathrm{Ar}^+$	penning ionization	–
$\mathrm{Ars} + \mathrm{Ar} \Longrightarrow \mathrm{Ar} + \mathrm{Ar}$	metastable quenching	–

2.2. Governing equations

The numerical model of the barrier discharge solves a pair of drift–diffusion equations for the electron density n_e and the mean electron energy ε ($n_\varepsilon = n_e\varepsilon$) given, respectively, as

$$\frac{\partial n_e}{\partial t} + \nabla \cdot \left[-n_e\left(\mu_e \boldsymbol{E}\right) - \boldsymbol{D}_e \nabla n_e\right] = R_e \tag{1}$$

and

$$\frac{\partial n_\varepsilon}{\partial t} + \nabla \cdot \left[-n_\varepsilon\left(\mu_\varepsilon \boldsymbol{E}\right) - \boldsymbol{D}_\varepsilon \nabla n_\varepsilon\right] + \boldsymbol{E} \cdot \boldsymbol{\Gamma_e} = R_\varepsilon. \tag{2}$$

In drift–diffusion equations, convection of electrons due to fluid motion is neglected. The drift–diffusion model adds the equations for electron transport in plasma. It specifies expressions for electron diffusivity D_e, electron mobility μ_e, electron energy diffusivity D_ε, electron energy mobility μ_ε, electric field $\boldsymbol{E}$, and electron flux $\boldsymbol{\Gamma_e}$. Term $(\boldsymbol{E}\cdot\boldsymbol{\Gamma_e})$ is the heating rate. In the model, there are also inputs for the electric potential and collisional power loss. In (1)–(2), the electron source is R_e and the energy loss due to inelastic collisions is R_ε. The electron diffusivity, energy mobility, and energy diffusivity are related to the electron mobility as

$$\begin{aligned} &D_e = \mu_e T_e, \quad \mu_\varepsilon = \tfrac{5}{3}\mu_e, \\ &D_\varepsilon = \mu_\varepsilon T_e. \end{aligned} \tag{3}$$

where T_e is an electron temperature given in volt. The electrostatic field is computed using the Poisson equation (3) by the finite element method using COMSOL Multi-physics software.

Te is an electron temperature in volt

The source coefficient in the above equations is determined by plasma chemistry, using rate coefficients. Suppose that there are M reactions that contribute to the growth or decay of electron density and P inelastic electron–neutral collisions. In general, P $\gg$ M.

Now, heavy species transport equation for non-electron species is shown by

$$\rho\frac{\partial}{\partial t}\left(w_k\right) + \rho(\boldsymbol{u}\cdot\nabla)w_k = \nabla \boldsymbol{j}_k + R_k. \tag{4}$$

where j_k is the diffusive flux vector, and w_k is the mass fraction of the k-th species. The heavy species (hs) transport interface, found under the

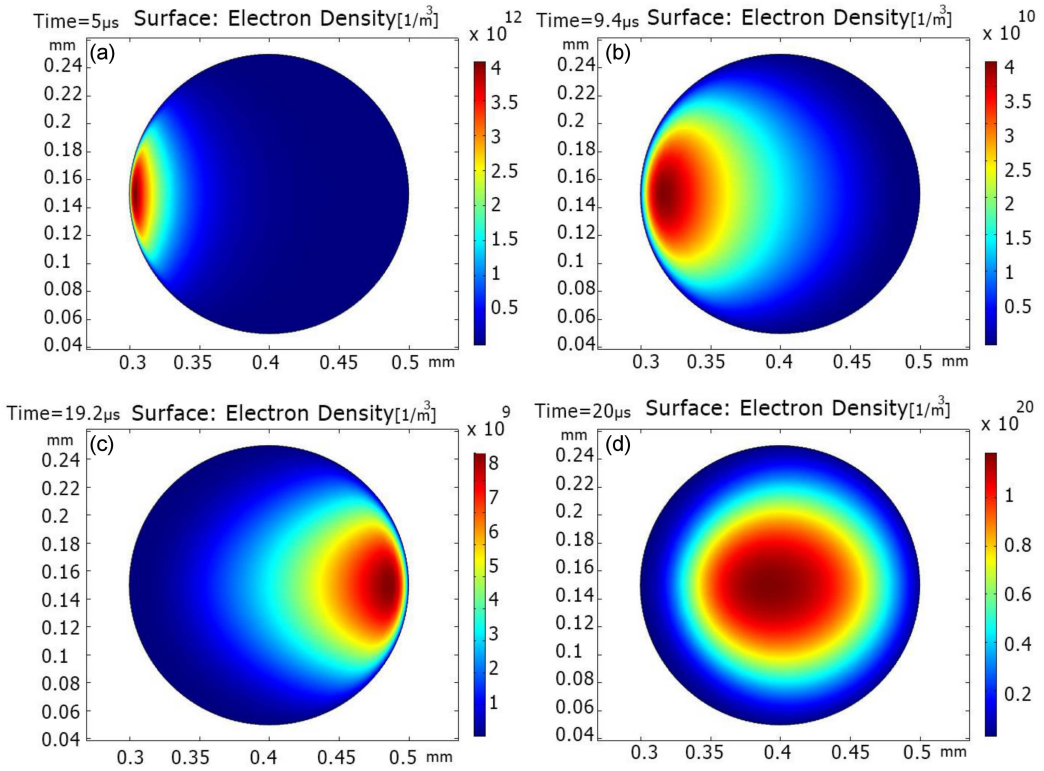

Fig. 7. Electron density changes by passing time indifferent region of bubble for 1000 applied voltage and 50 kHz of frequency. Electron density at $t = 5$ μs was 4×10^{12} m^{-3} (a), at $t = 9.4$ μs was 3.6×10^{10} m^{-3} (b), at $t = 19.2$ μs was 8.3×10^{9} m^{-3} (c), at $t = 20$ μs was 1.8×10^{10} m^{-3} (d).

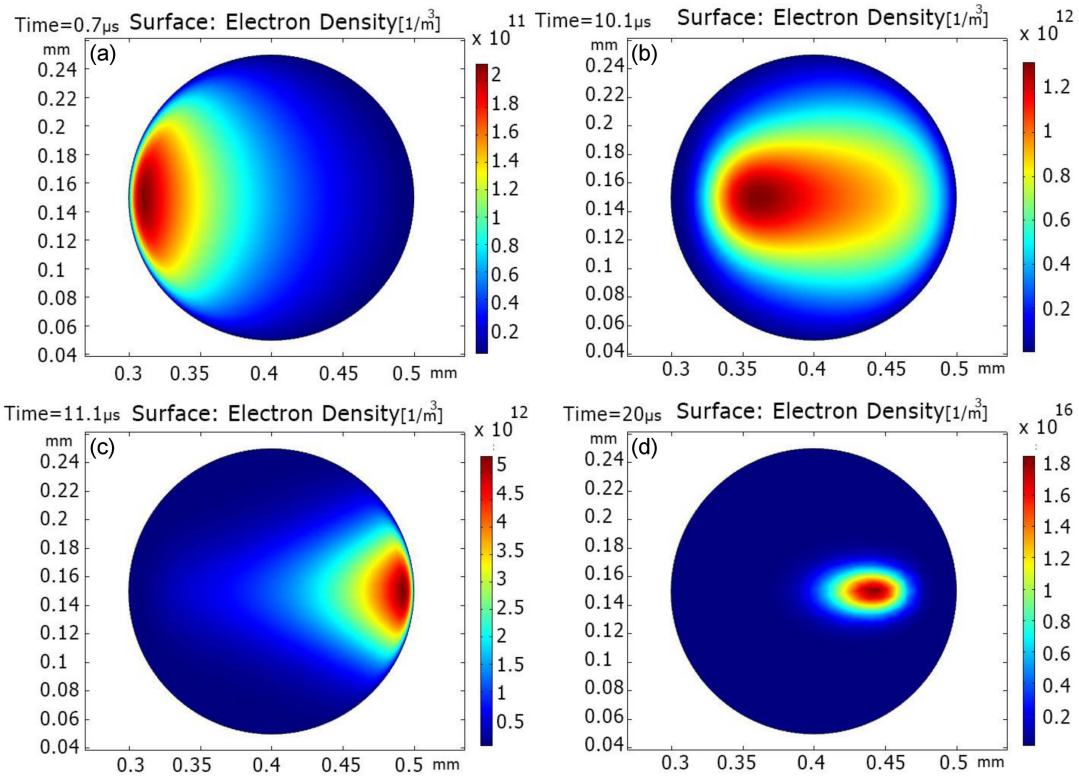

Fig. 8. Electron density changes by passing time in different region of bubble for 1500 applied voltage and 50 kHz of frequency. Electron density at $t = 0.7$ μs was 2×10^{11} m^{-3} (a), at $t = 10.1$ μs was 1.2×10^{12} m^{-3} (b), at $t = 11.7$ μs was 2.5×10^{13} m^{-3} (c), at $t = 20$ μs was 1.8×10^{16} m^{-3} (d).

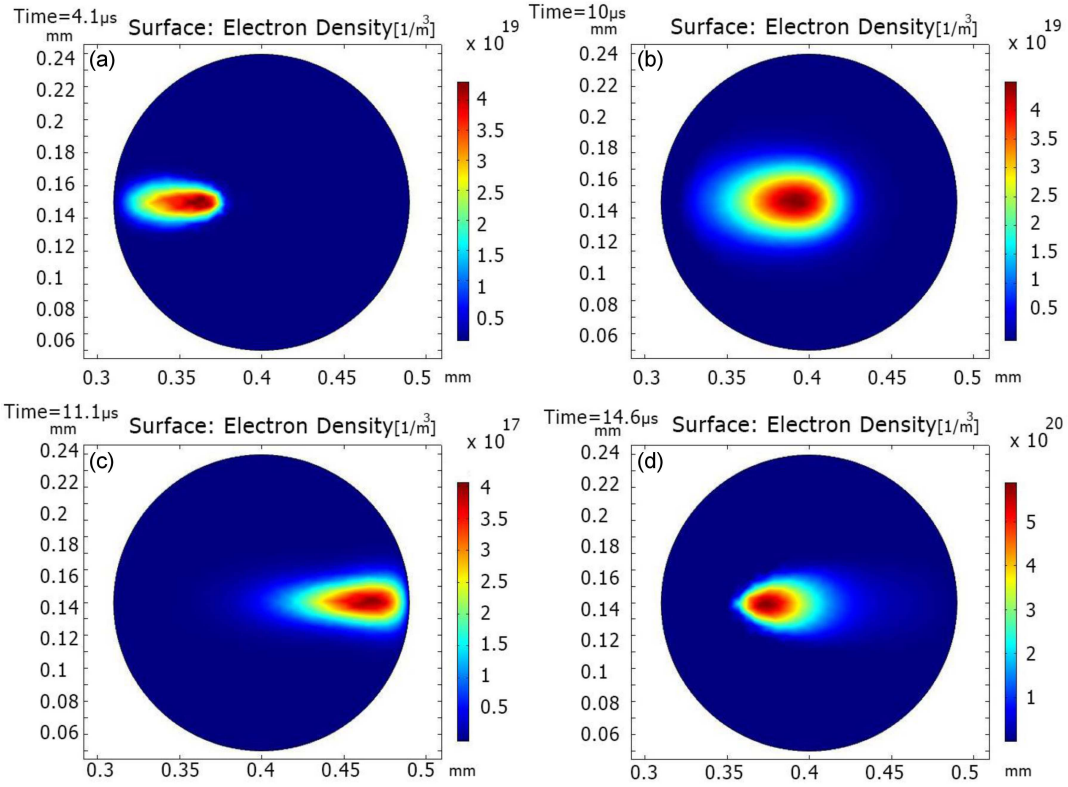

Fig. 9. Electron density changes by passing time indifferent region of bubble for 2000 applied voltage and 50 kHz of frequency. Electron density at $t = 4.1$ μs was 4.29×10^{19} m^{-3} (a), at $t = 10$ μs was 4.48×10^{19} m^{-3} (b), at $t = 11.1$ μs was 4.06×10^{17} m^{-3} (c), at $t = 14.6$ μs was 5.87×10^{20} m^{-3} (d).

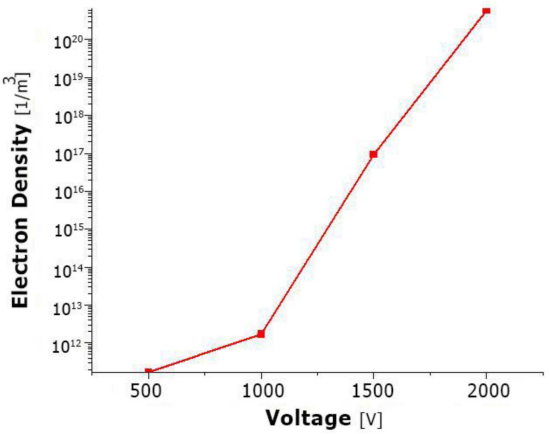

Fig. 10. Voltage changes with electron density.

plasma branch when adding a physics interface, adds electron impact reactions, gas phase reactions, and species and surface reactions to plasma models. The electrostatics interface found under the AC/DC branch is used to compute the electric field, electric displacement field, and potential distributions in dielectrics under conditions where the electric charge distribution is explicitly prescribed. The physics interface solves Gauss' law for the electric field using the scalar electric potential as the dependent variable.

The electrostatic field is solved according to

$$-\varepsilon_0\varepsilon_r\nabla\cdot\nabla V = \rho. \tag{5}$$

This equation demonstrates charge conservation for defining the constitutive relation for the electric displacement field and its associated properties, such as the relative permittivity.

The space charge density ρ is automatically computed based on the plasma chemistry specified in the model using

$$\rho = q\left(\sum\nolimits_{k=1}^{N} Z_k n_k - n_e\right) \tag{6}$$

with q — electric charge.

2.3. Boundary conditions

Electrons are lost to the wall due to random motion within a few mean free paths of the wall and gained due to secondary emission effects, resulting in the following boundary condition for the electron flux

$$\boldsymbol{n}\cdot\boldsymbol{\Gamma}_e = \tfrac{1}{2}V_{e,th}\,n_e - \sum\nolimits_p \gamma_p\left(\boldsymbol{\Gamma}_p\cdot\boldsymbol{n}\right) \tag{7}$$

with $\boldsymbol{n}$ being a unit vector normal to the surface, and $V_{e,th}$ is the thermal velocity of electron.

In the case of the electron energy flux density $\boldsymbol{\Gamma}_\varepsilon{=}n_\epsilon(\mu_\varepsilon\boldsymbol{E}){-}\nabla(\boldsymbol{D}_\varepsilon n_\varepsilon)$, the boundary condition is

$$\boldsymbol{n}\cdot\boldsymbol{\Gamma}_\varepsilon = \tfrac{5}{6}V_{e,th}\,n_\varepsilon - \sum\nolimits_p \varepsilon_p\gamma_p\left(\boldsymbol{\Gamma}_p\cdot\boldsymbol{n}\right). \tag{8}$$

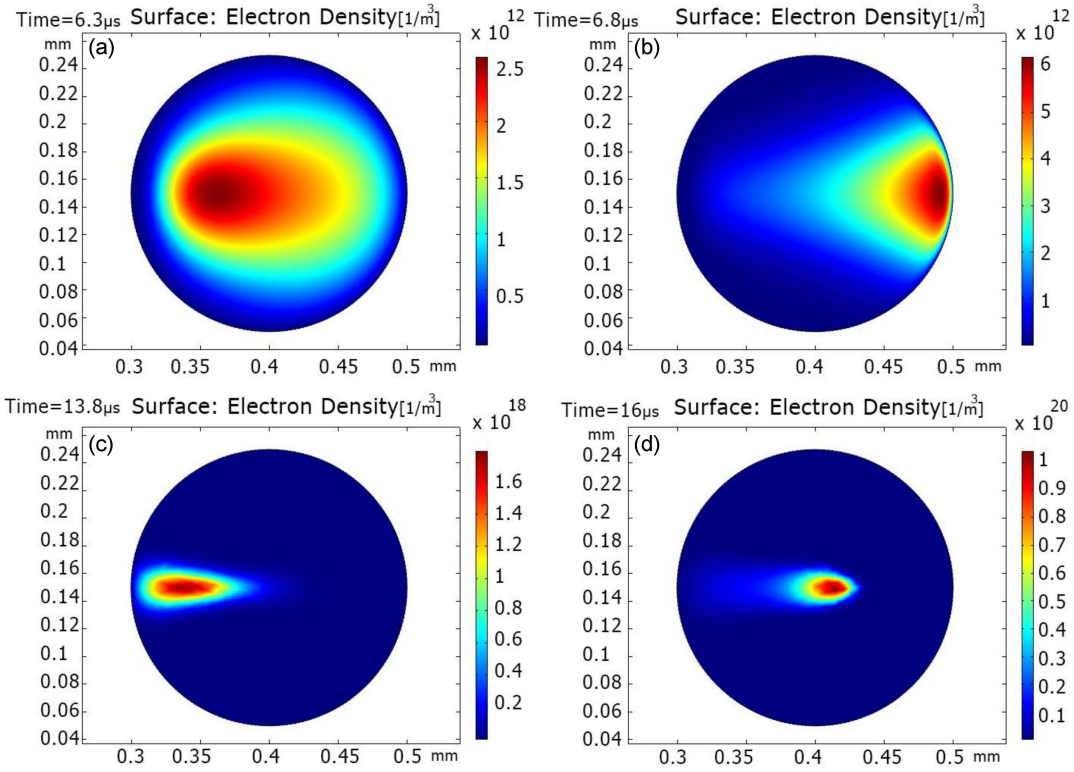

Fig. 11. Electron density changes by passing time in different region of bubble for 1500 V applied voltage and frequency= 80 kHz. Electron density at $t = 6.3$ μs was 2.5×10^{12} m^{-3} (a), at $t = 6.8$ μs was 6×10^{12} m^{-3} (b), at $t = 13.8$ μs was 1.6×10^{18} m^{-3} (c), at $t = 16$ μs was 1×10^{20} m^{-3} (d).

The second term on the right-hand side of (7) is the gain of electrons due to secondary emission effects, with γ_p being the secondary emission coefficient. The second term in (8) is the secondary emission energy flux, with ε_p being the mean energy of the secondary electrons.

The set of reactions and collisions considered in the simulated model are given in Table I.

3. Results

One of the electrodes is taken into account as the ground in the modeling of the arc and dielectric barrier discharge, while a sinusoidal voltage is provided to the other electrode. The initial electron density is assumed to be 10^{13} m^{-3}. We examine the impact of variations in the parameters of frequency, voltage, dielectric thickness, bubble radius, and electron density. Time-varying arc discharge characteristics, such as electron density, electric field, and potential, were investigated.

First, the examined modification of dielectric barrier discharge parameters is presented as follows.

3.1. Dielectric barrier discharge for single bubble

3.1.1. Voltage

The dynamic evolution of electron density over time at different voltages is depicted in Figs. 7–9. Warmer colors represent a higher intensity.

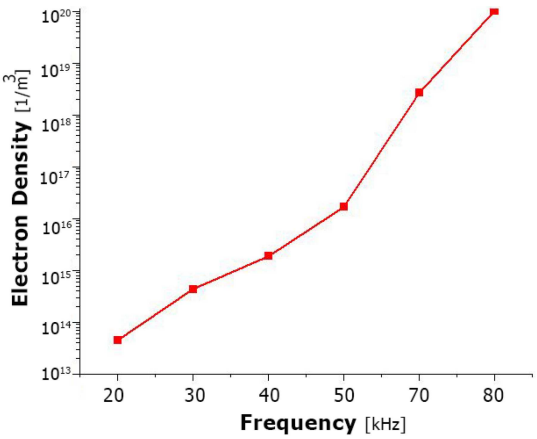

Fig. 12. Frequency changes with electron density.

A frequency of 50 kHz, a bubble radius of 0.1 mm, and a gap distance of 1 mm were used as constants for the simulation. Figure 7 illustrates the resulting electron density at a voltage of 1000 V; at the first time (t=5 μs), the initial electron density is 4×10^{12} m^{-3} (Fig. 7a), and at the last time ($t = 20$ μs), the electron density is equal to 10^{10} m^{-3} (Fig. 7d). Figure 7 illustrates the behavior of the electron density over time at various voltages between 500 and 1000 V. The same non-uniform electron density changes have been observed by W. Tian et al. [36] by 20 kV applied voltage and 4 mm of bubble

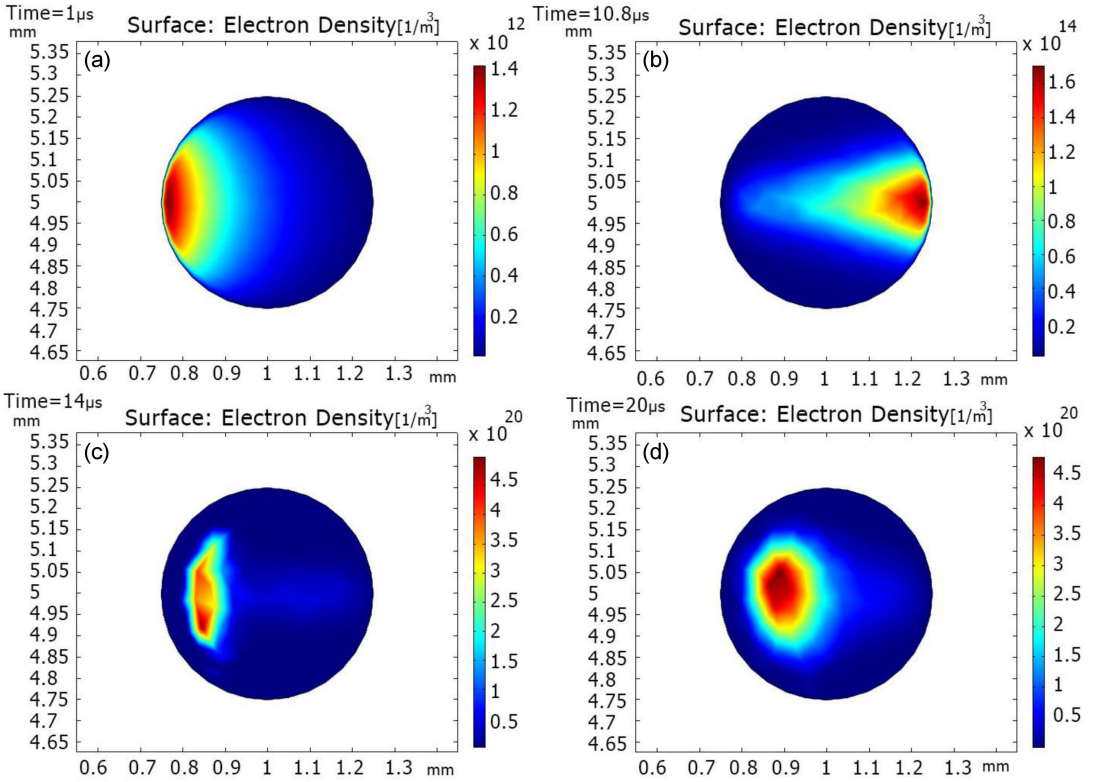

Fig. 13. Electron density changes by passing time in different region of bubble for dielectric thickness = 0.5 mm. Electron density at $t = 1$ μs was 1.4×10^{12} m^{-3} (a), at $t = 10.8$ μs was 1.6×10^{14} m^{-3} (b), at $t = 14$ μs was 4.5×10^{20} m^{-3} (c), at $t = 20$ μs was 4.5×10^{20} m^{-3} (d).

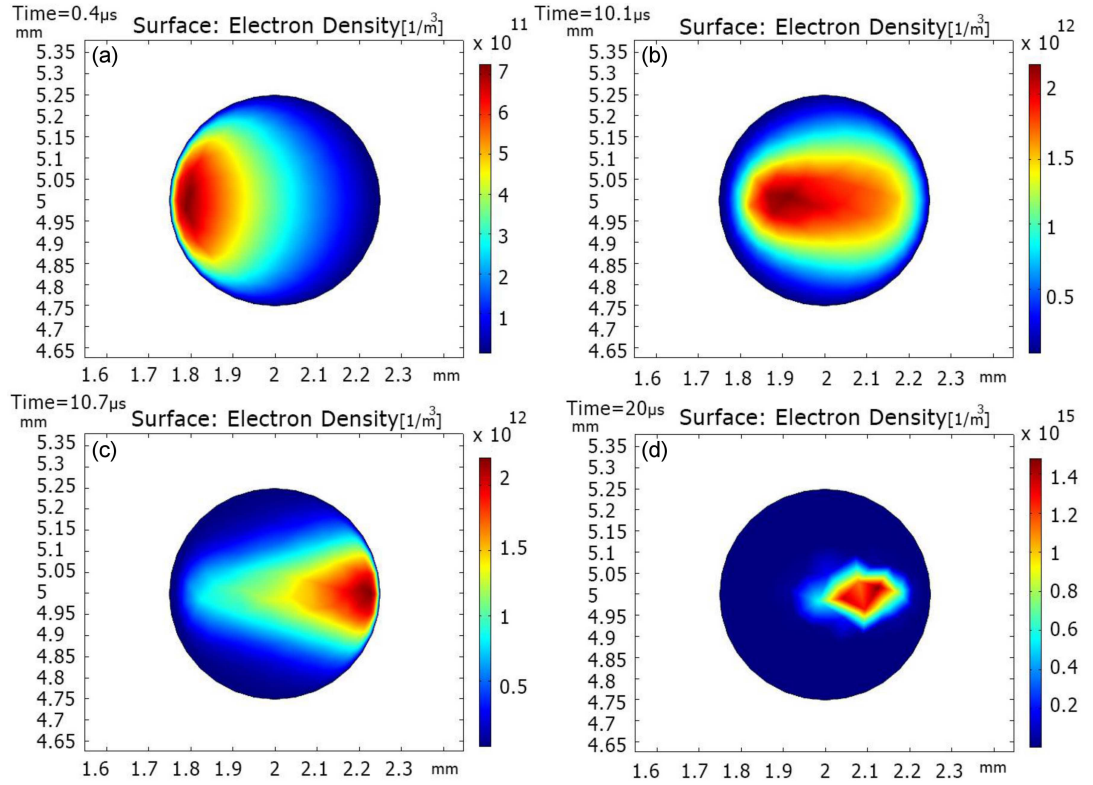

Fig. 14. Electron density changes by passing time in different region of the bubble for dielectric thickness = 1.5 mm. Electron density at $t = 0.4$ μs was 7×10^{11} m^{-3} (a) at $t = 10.1$ μs was 5×10^{12} m^{-3} (b), at $t = 10.7$ μs was 1.8×10^{14} m^{-3} (c), at $t = 20$ μs was 1.4×10^{15} m^{-3} (d).

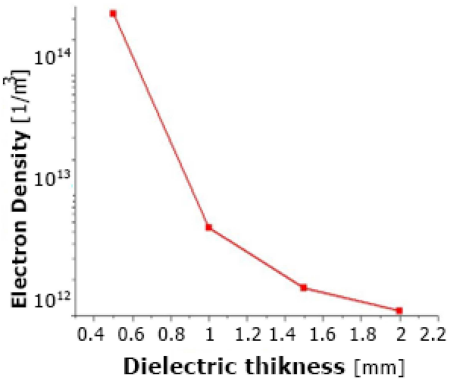

Fig. 15. Dielectric thickness changes with electron density.

diameter for times of bubble diameter for times $t = 0.7$, 1, 1.5, 1.9, 2.5, 4.4, 5.6, 10 ns. Figures 7 and 8 show electron density at voltages of 1500 V and 2000 V, respectively; at $t = 20$ μs, the electron density is 10^{16} m^{-3} (Fig. 7d) and 10^{20} m^{-3} (Fig. 7d). A direct relation between time and density has been shown by D. Levko et al. [37] in the shorter period of time ($t = 1$, 2, 3.6, 4.4 ns) by applying a voltage of -9 kV and DC, and by W. Ning et al. [38] by applying -13 kV and DC in the bubble of 0.1 mm diameter for times $t = 0.4$, 0.5, 0.6, 1.7 ns. In Fig. 7c and 7d, dielectric barrier discharge has a very important factor called surface charge. Surface charges cause an electric field against an external field. The alternating external voltage could amplify that electrical field in its half cycle. The alignment of both external and internal electric fields results in strength at the center of the bubble. Also, at $t = 19.2$ μs, the field is almost zero, and the density is low. In this case, the internal field is effective and causes the electron density to move toward the center.

A voltage given to the electrodes creates an electric field between them, and as the voltage increases, so does the electric field. Therefore, there can be a greater increase in the energy of particle collisions. As a result, increased ionization causes the development of the plasma zone and increased creation of free electrons. As can be seen in Fig. 10, the results demonstrate that increasing voltage causes the electron density to rise linearly. In this study micro-second period is employed because of low applied voltage, in comparison with the same works, as nanosecond periods of time were not enough to initiate plasma — no electron density increase is detected in a short nanosecond period.

3.1.2. Frequency

The frequency range was from 20 to 80 kHz, with constant parameters: voltage of 1500 V, bubble radius of 0.1 mm, and gap distance of 1 mm. Figure 11 shows the resulting electron density for these parameters — at the frequency of 80 kHz last time ($t = 16$ μs) the electron density value is 10^{20} m^{-3} (Fig. 11d).

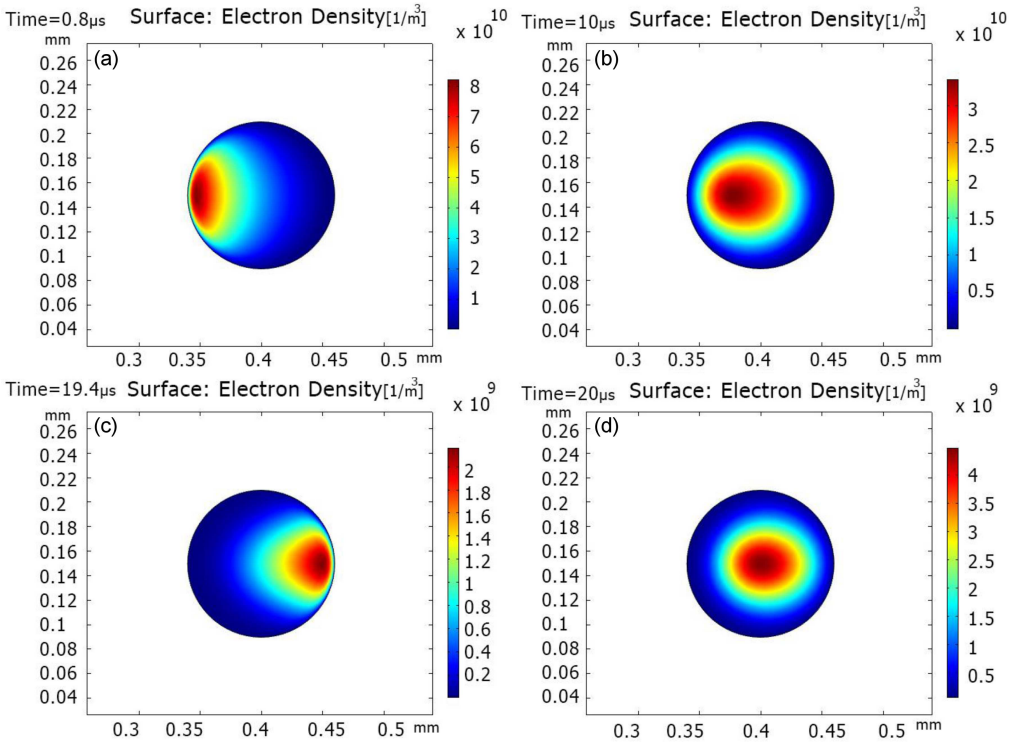

Fig. 16. Electron density changes by passing time in different region of bubble for radius = 0.06 mm. Electron density at $t = 0.8$ μs was 8.21×10^{10} m^{-3} (a), at $t = 10$ μs was 3.34×10^{10} m^{-3} (b), at $t = 19.4$ μs was 2.16×10^{9} m^{-3} (c), at $t = 20$ μs was 4.46×10^{9} m^{-3} (d).

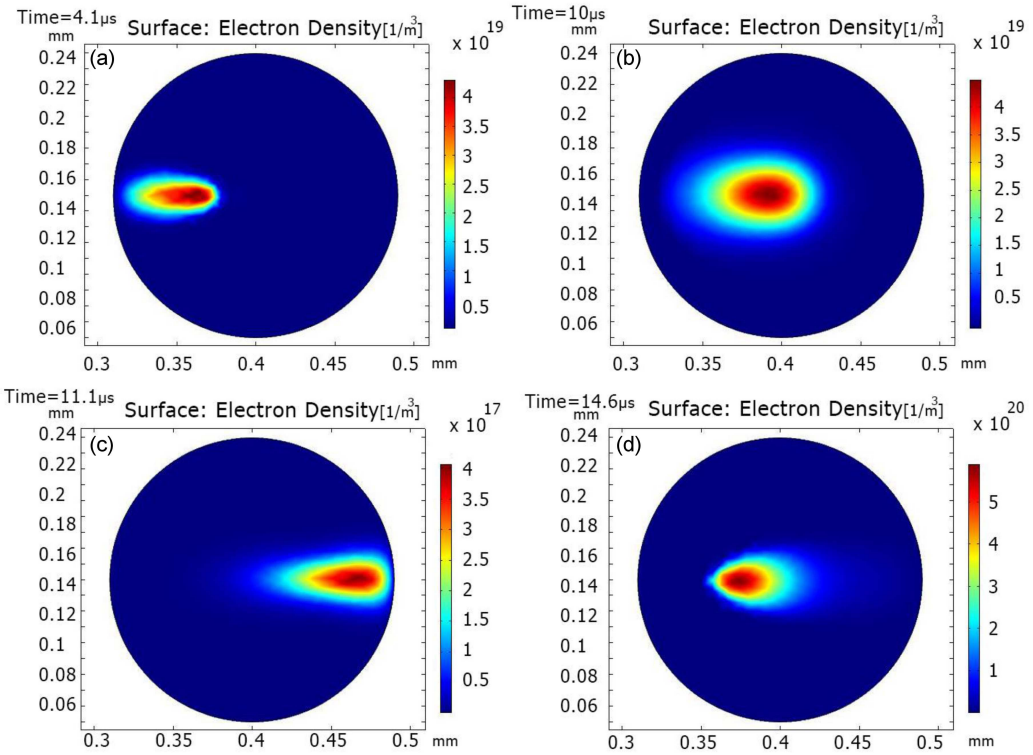

Fig. 17. Electron density changes by passing time in different region of bubble for radius = 0.09 mm. Electron density at $t = 4.1$ μs was 4.29×10^{19} m^{-3} (a), at $t = 10$ μs was 4.48×10^{19} m^{-3} (b), at $t = 11.1$ μs was 4.06×10^{17} m^{-3} (c), at $t = 14.6$ μs was 5.87×10^{20} m^{-3} (d).

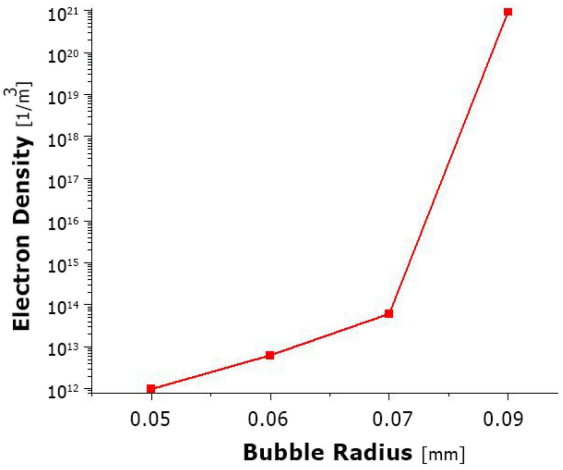

Fig. 18. Bubble radius changes with electron density.

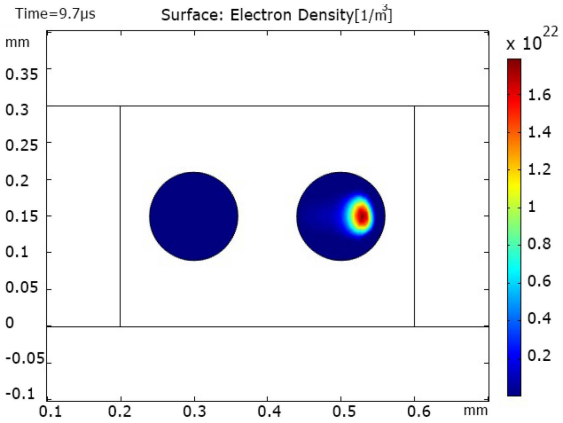

Fig. 19. Electron density distribution in two bubbles geometry.

The results demonstrated that when the frequency increases, electron density also increases (see Fig. 12). The direction of the electric field would change, and so would the motion of the electrons. The power source as the controller of this procedure by a parameter called frequency could limit the electron path. This limitation causes more electron trapping and more electron density inside the bubble.

3.1.3. Dielectric thickness

In this section of the simulation, the dielectric thickness is assumed to be between 0.5 and 1.5 mm with constant values for the voltage, frequency, and bubble radius of 1800 V, 50 kHz, and 0.1 mm, respectively. Figures 13 and 14 show the changes in the electron density of 10^{20} m^{-3}at a dielectric thickness of 0.5 and the electron density of 10^{15} m^{-3} at a dielectric thickness of 1.5 mm. The electron density decreases with increasing dielectric thickness, as shown in Fig. 15.

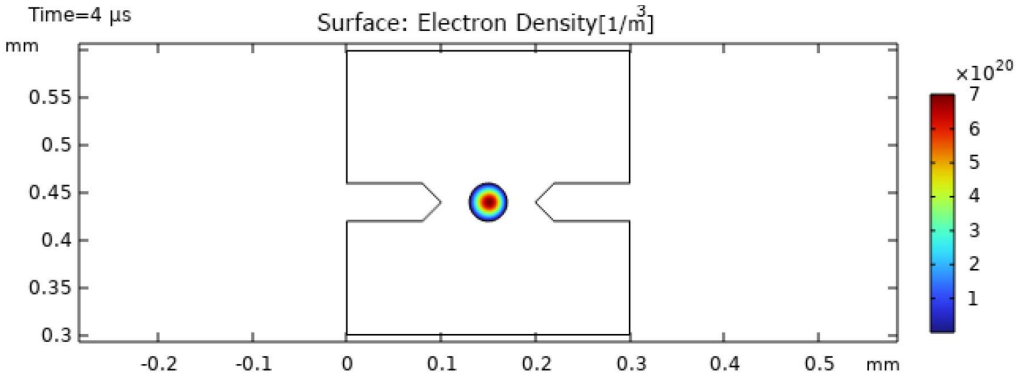

Fig. 20. Two-dimensional schematic of electron density for arc discharge simulation.

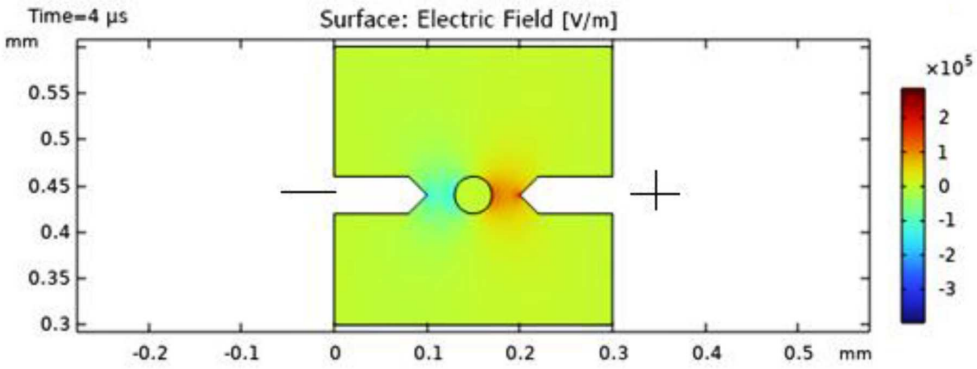

Fig. 21. Two-dimensional schematic of the electric field for arc discharge simulation.

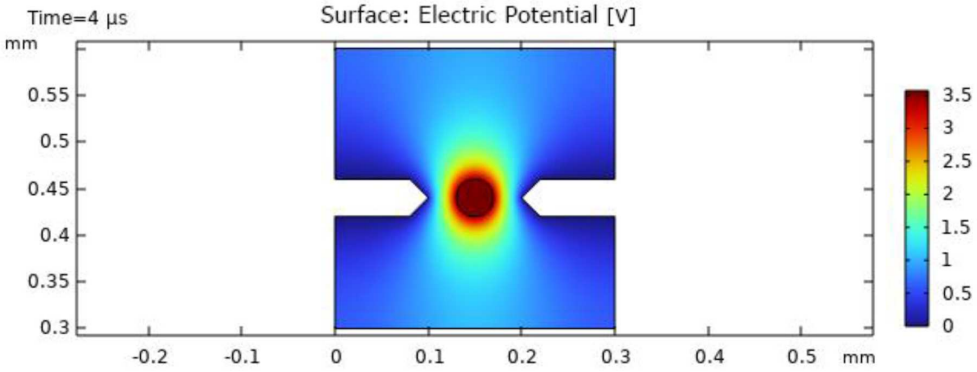

Fig. 22. Two-dimensional schematic of electric potential for arc discharge simulation.

Increasing the dielectric thickness would decrease the capacitance of the system so lower electrical charges on electrodes and lower electric field lead to less electron density.

3.1.4. Bubble radius

In this part, the bubble size is considered to be 0.06 mm and 0.09 mm with constant electric potential of 2000 V, frequency of 50 kHz, and dielectric thickness of 0.5 mm. Figures 16–18 illustrate how expanding the bubble radius results in an increase in electron density.

Some noticeable results of simulation of double bubbles geometry are shown in the following.

3.2. Dielectric barrier discharge for double bubble (electron density)

By applying frequency of 2000 V and 50 kHz, no plasma formed in one of the bubbles as the electron density of the other bubble due to the formation of plasma made an electric sheath that prevent any other plasma from forming. That sheath abated the total electric field, so such

a result was predicted to happen. Figure 19 shows the electron density distribution in the described geometry.

In the following, the simulation results of applying an arc discharge are presented.

3.3. Arc discharge for single bubble

3.3.1. Electron density

In this simulation, all the variables, such as electric field, electric potential, and electron density, have been studied.

Figure 20 shows the change in electron density. The initial electron density was 10^{13} m^{-3}, increased over time, and reached the value of 10^{20} m^{-3}. The increase in the electron density is a sign that plasma is forming inside the bubble.

3.3.2. Electric field

The electrical discharge initiates at the bubble-liquid boundary, and the field at the bubble-water boundary is very strong. As Fig. 21 shows, there is an accumulation of charge at the sharp points, and as a result, the electric field increases.

3.3.3. Electric potential

For some electrons, pure water acts like a dielectric and causes the accumulation of charge on the outer surface of the bubble, and as a result, the electric potential increases. Also, due to the electric discharge inside the bubble, it becomes electrically conductive and behaves like a conductive sphere, in which case the entire plasma environment becomes of the same potential (see Fig. 22).

4. Conclusions

Two-dimensional simulations of a single bubble with a DBD and arc plasma structures are studied using the finite element method (FEM). The effect of changes in some parameters, including voltage, frequency, dielectric thickness, and bubble radius, on electron density and the electron density by time in arc discharge with constant voltage has been studied. The results show that increasing voltage, frequency, and bubble radius have a direct effect on the increase in electron density. Electron density as a sign of plasma region evidently has been changed by these parameters — it is the same effect of "step voltage" as when lightning strikes or approaches an uninsulated live wire lying on the ground. The larger the dimension, the greater the potential difference, and thus the easier ionization. The formation of plasma in a bubble inside water is possible by selecting the appropriate frequency and voltage. It is more possible for micro-size bubbles more than nano-size bubbles. Creating a high voltage difference between a nanometer-diameter sphere is more difficult than a micrometer bubble and requires a stronger generator due to Paschen's curve, which says that as the bubble size becomes smaller, the formation of the discharge requires a higher voltage.

References

[1] S.K. Pankaj, C. Bueno-Ferrer, N.N. Misra, V. Milosavljević, C.P. O'Donnell, P. Bourke, K.M. Keener, P.J. Cullen, *Trends Food Sci. Technol.* **35**, 5 (2014).

[2] B. Jiang, J. Zheng, S. Qiu, M. Wu, Q. Zhang, Z. Yan, Q. Xue, *Chem. Eng. J.* **236**, 348 (2014).

[3] T. Von Woedtke, S. Emmert, H.R. Metelmann, S. Rupf, K.D. Weltmann, *Phys. Plasmas* **27**, (2020).

[4] A. Seifalinezhad, M. Bahreini, M.M.H. Matin, S.H. Tavassoli, *J. Lasers Med. Sci.* **10**, 64 (2019).

[5] M. Bahreini, *J. Lasers Med. Sci.* **6**, 51 (2015).

[6] J.S. Park, I. Han, E.H. Choi, *AIP Adv.* **9**, 075125 (2019).

[7] Q. Wang, Y. Sun, S. Zhang, Y.-W. Ding, M. Gao, *AIP Adv.* **12**, 075115 (2022).

[8] V. Scholtz, E. Kvasničková, J. Julák, *Acta Phys. Pol. A* **124**, 62 (2013).

[9] J. Jain, J. Moreno, R. Andaur et al., *AIP Adv.* **7**, 085121 (2017).

[10] S.S. Akdeniz, E. Beyler, Y. Korkmaz, E. Yurtcu, U. Ates, K. Araz, F.I. Sahin, O.Y. Torun, *Clin. Oral Investig.* **22**, 867 (2018).

[11] J.D. Holcomb, *Facial Plast. Surg. Clin. North Am.* **28**, 67 (2020).

[12] D.M. Hamdy, H.A. Osman, A.G. Hassabo, *J. Text. Color. Polym. Sci.* **19**, 1 (2022).

[13] M. Ito, J.S. Oh, T. Ohta, M. Shiratani, M. Hori, *Plasma Process. Polym.* **15**, 1700073 (2018).

[14] R. Mandal, A. Singh, A.P. Singh, *Trends Food Sci. Technol.* **80**, 93 (2018).

[15] N. Puač, M. Gherardi, M. Shiratani, *Plasma Process. Polym.* **15**, 1700174 (2018).

[16] M. Fojlaley, E. Imani, *Eur. J. Mol. Clin. Med.* **08**, 1840 (2021).

[17] T. Namihira, D. Wang, H. Akiyama, *Acta Phys. Pol. A* **115**, 953 (2009).

[18] L. Lin, X. Li, J. Zhou, J. Zou, J. Lai, Z. Chen, J. Shen, H. Xu, *J. Taiwan Inst. Chem. Eng.* **122**, 311 (2021).

[19] A. Safi, M. Bahreini, S.H. Tavassoli, *Opt. Spectrosc.* **120**, 367 (2016).

[20] S.C. Andola, R. Niranjan, R. Srivastava, *Nucl. Instrum. Methods Phys. Res. A* **1004**, 165362 (2021).

[21] J.E. Foster, *Phys. Plasmas* **24**, 055501 (2017).

[22] P.J. Bruggeman, M.J. Kushner, B.R. Locke et al., *Plasma Sources Sci. Technol.* **25**, 053002 (2016).

[23] Y.M. Zhao, A. Patange, D.W. Sun, B. Tiwari, *Compr. Rev. Food Sci. Food Safety* **19**, 3951 (2020).

[24] Z. Zou, R. Han, C. Lu, *Plasma Process. Polym.* **18**, 2000139 (2020).

[25] R. Zhou, R. Zhou, P. Wang, Y. Xian, A. Mai-Prochnow, X. Lu, P.J. Cullen, K. (Ken) Ostrikov, K. Bazaka, *J. Phys. D Appl. Phys.* **53**, 303001 (2020).

[26] Y. Tian, K. Wang, S. Wu, R. Ma, Q. Zhang, J. Zhang, J. Fang, in: *IEEE Int. Conf. on Plasma Science (ICOPS)*, Banff (Canada) 2016.

[27] P.S.G. Subramanian, A. Jain, A.M. Shivapuji, N.R. Sundaresan, S. Dasappa, L. Rao, *Plasma Process. Polym.* **17**, 1 (2020).

[28] D. Guo, H. Liu, L. Zhou, J. Xie, C. He, *J. Sci. Food Agric.* **101**, 4891 (2021).

[29] R.P. Guragain, H.B. Baniya, S.P. Pradhan, B.P. Pandey, D.P. Subedi, *AIP Adv.* **11**, 125304 (2021).

[30] P. Dimitrakellis, M. Giannoglou, Z.M. Xanthou, E. Gogolides, P. Taoukis, G. Katsaros, *Plasma Process. Polym.* **18**, 2100030 (2021).

[31] S.N. Kutlu, F. Canatan, A. Güleç, in: *2018 Medical Technologies National Congress (TIPTEKNO)*, 2018.

[32] N. Vichiansan, K. Leksakul, P. Chaopaisarn, D. Boonyawan, *AIP Adv.* **11**, 035040 (2021).

[33] A. Wright, M. Taglioli, F. Montazersadgh, A. Shaw, F. Iza, H.C.H. Bandulasena, *Chem. Eng. Res. Design* **144**, 159 (2019).

[34] Y. Wang, Z. Wang, H. Yang, X. Zhu, *J. Food Eng.* **286**, 110117 (2020).

[35] Z. Zhao, X. Wei, R. Guan, H. Nie, B. Zhu, Y. Yao, in: *IEEE Trans. Plasma Sci.* **50**, 1160 (2022).

[36] W. Tian, M.J. Kushner, *J. Phys. D Appl. Phys.* **47**, 165201 (2014).

[37] D. Levko, L. Raja, *J. Phys. D Appl. Phys.* **49**, 285205 (2016).

[38] W. Ning, J. Lai, J. Kruszelnicki, J.E. Foster, D. Dai, M.J. Kushner, *Plasma Sources Sci. Technol.* **30**, 015005 (2021).